

# Heat and fluid flow in additive manufacturing—Part I: Modeling of powder bed fusion

T. Mukherjee<sup>a</sup>, H.L. Wei<sup>a</sup>, A. De<sup>b</sup>, T. DebRoy<sup>a,\*</sup>

<sup>a</sup> Department of Materials Science and Engineering, The Pennsylvania State University, University Park, PA 16802, USA

<sup>b</sup> Department of Mechanical Engineering, Indian Institute of Technology, Bombay, 400076, India

## ARTICLE INFO

### Keywords:

Powder bed fusion  
Heat transfer and fluid flow  
Marangoni convection  
Packing efficiency  
Travelling grid

## ABSTRACT

Structure and properties of components made by the powder bed fusion (PBF) additive manufacturing (AM) are often optimized by trial and error. This procedure is expensive, time consuming and does not provide any assurance of optimizing product quality. A recourse is to build, test and utilize a numerical model of the process that can estimate the most important metallurgical variables from the processing conditions and alloy properties. Here we develop and test a three-dimensional, transient, heat transfer and fluid flow model to calculate temperature and velocity fields, build shape and size, cooling rates and the solidification parameters during PBF process. This model considers temperature dependent properties of the powder bed considering powder and shielding gas properties, packing efficiency and powder size. A rapid numerical solution algorithm is developed and tested to calculate the metallurgical variables for large components fabricated with multiple layers and hatches rapidly. Part I of this article describes the model, solution methodology, powder bed properties, and model validation. The applications of the model for four commonly used alloys are presented in part II.

## 1. Introduction

In laser-assisted powder bed fusion (PBF) process, parts are built by progressively melting thin layers of alloy powders by a laser beam [1]. Structure and properties of these components are affected by the metallurgical variables such as transient temperature fields, cooling rates and solidification parameters. These metallurgical variables depend on process parameters such as laser power, wavelength, power distribution, travel speed, layer thickness, hatch spacing, powder shape and size and the alloy used [1]. Currently, the structure and properties of the components are often optimized by trial and error without any guiding scientific framework. This method is expensive, time consuming, and provides no assurance of achieving the desired product attributes [2,3]. A recourse is to develop, test and utilize theoretical models that enable users to specify various additive manufacturing (AM) process parameters and alloy properties to obtain the important metallurgical variables such as the transient temperature fields, cooling rates and solidification parameters. In short, when adequately tested with experimental data, these models help to fabricate defect free, structurally sound and reliable components based on scientific principles.

Several attempts have been made to calculate important metallurgical variables in PBF. Finite element based heat conduction models [4,5] can calculate temperature fields, build shape and size,

cooling rates and solidification parameters. However, these models neglect the effects of the convective flow of liquid metal inside the molten pool driven by the surface tension gradient on the top surface of the pool. Since convection is the main mechanism of heat transfer within the liquid pool, such calculations result in erroneous temperature gradients, unrealistic cooling rates and solidification growth rates. Manvatkar et al. [6] showed that the cooling rates are overestimated by a factor of two when the molten metal convection is ignored during laser-assisted direct energy deposition. Heat transfer and fluid flow models [7,8] are computationally intensive and various simplifications are often made to make them tractable. Careful consideration of thermophysical properties of the powder bed taking into account powder size and/or packing efficiency is needed to correctly simulate experimental results. Powder scale models [9–12] using level set method or volume of fluid method consider both molten metal convection and correct powder bed properties. However, these models are computationally intensive and often restricted to two-dimensional calculations. In addition, they have not been applied to examine the manufacture of real components with multiple layers and hatches.

Here, we develop and test a three-dimensional, transient heat transfer and fluid flow model for multiple layers and hatches PBF process. The model solves the equations of conservation of mass, momentum and energy in transient, three-dimensional form. These governing equations are

\* Corresponding author.

E-mail address: [debroy@psu.edu](mailto:debroy@psu.edu) (T. DebRoy).

discretized using control volume method in a solution domain that consists of the substrate, powder bed and solidified build. Effects of the molten metal convection are considered in the calculations. The temperature dependent thermo-physical properties of the powder bed are calculated considering the size of the powder and packing efficiency of the powder bed. A traveling grid system along the direction of scanning has been developed to achieve high computational efficiency while limiting memory requirements for the simulation of large transient problems in builds involving multiple layers and hatches. The calculated results are compared with independent experimental data.

Due to the complexity of the problem and the applicability of the traveling grid algorithm to save computational time and memory requirements in large related three-dimensional transient problems, the work is divided into two parts. In this paper (part I) the development of the model, discretization of the governing equations, calculation of powder bed properties and the development and testing of a computationally efficient solution technique are presented. In an accompanying paper (part II) the application of the model to laser-assisted PBF of four commonly used alloys, stainless steel 316, Ti-6Al-4V, Inconel 718 and AlSi10Mg are discussed.

## 2. Numerical heat transfer and fluid flow model

The solution domain consists of the substrate, powder bed and multi-layer multi-hatch build as shown in Fig. 1. The scanning, hatching and building directions are indicated by X, Y and Z, respectively. For simplicity, unidirectional scanning strategy is used where the laser beam travels only along the positive X-direction for all layers and hatches. After a particular hatch is completed, the laser beam shifts along the positive Y-axis by a distance equal to the hatch spacing. After the completion of all hatches in a particular layer, the laser beam shifts along the positive Z-axis by a distance equal to the layer thickness since the powder bed is lowered by the same distance in the actual process. The same process continues until all hatches and layers are completed. Heat transfer calculations are done in the entire solution domain. However, fluid flow calculations are restricted inside a smaller domain containing the molten pool and its adjacent regions to save the total computational time.

### 2.1. Assumptions

The following simplifying assumptions are made to make the computational work tractable.

(a) Densities of powder, solid and liquid alloys are assumed to be

independent of temperature except for the calculation of the buoyancy force. This assumption is known as the Boussinesq approximation and is widely used in the calculations of buoyancy driven flow [2,13].

- (b) The surfaces of the growing layers and hatches are assumed to be flat.
- (c) The liquid metal flow is assumed to be incompressible and Newtonian. The turbulent flow in the molten pool is considered through the use of the enhanced thermal conductivity and viscosity of the liquid metal [14].
- (d) The loss of alloying elements due to vaporization [15] and its effects on both heat loss and composition change are not considered in the calculations.

### 2.2. Governing equations and volumetric heat source

The heat transfer and fluid flow model is applied in a 3D Cartesian co-ordinate system and it solves the equations of conservation of mass, momentum and energy [15–18] to calculate enthalpy, three components of velocity and pressure.

By dividing the total enthalpy into the sensible heat and the latent heat of fusion, the energy conservation equation is written as:

$$\frac{\partial h}{\partial t} + \frac{\partial(u_i h)}{\partial x_i} = \frac{\partial}{\partial x_i} \left( \alpha \frac{\partial h}{\partial x_i} \right) - \frac{\partial \Delta H}{\partial t} - \frac{\partial(u_i \Delta H)}{\partial x_i} + S_v \quad (1)$$

where  $h$  is the sensible heat,  $t$  is the time,  $\alpha$  and  $\Delta H$  are the thermal diffusivity and the latent heat of fusion of the alloy, respectively,  $u_i$  and  $x_i$  are the velocity components and the distance along the  $i$  direction, respectively and  $S_v$  is the source term to account for the volumetric heat source. In PBF-AM, the laser beam undergoes multiple reflections inside the powder layers [1]. Therefore, a 3D volumetric heat source is considered here. The heat source is characterized by the laser power ( $P_L$ ), laser beam radius ( $r_b$ ) and a power distribution factor ( $d$ ):

$$S_v = \frac{d \epsilon P_L}{\pi r_b^2 \lambda} \exp \left[ -\frac{d(x_b^2 + y_b^2)}{r_b^2} \right] \quad (2)$$

where  $x_b$  and  $y_b$  are the X and Y distances from the axis of the laser beam, respectively and  $\lambda$  is the powder layer thickness. The distribution factor,  $d$  varies between 1 and 3 depending on the spatial distribution of the power of the laser beam on a particular XY-plane [1]. The higher the distribution factor, the higher the peak power. The distribution of the laser power is uniform along z-direction throughout the powder layer thickness and  $\epsilon$  is the heat absorption coefficient. The absorption coefficient is high inside the powder layer due to the multiple reflections of the laser beam. For example, a value of  $\epsilon = 0.7$  was reported for stainless steel 316 [1]. However, as the powder melts the absorption coefficient drops to the Fresnel absorptivity, which is 0.3 for stainless steel 316 irradiated by a Nd-YAG laser [1].

Velocities of the metal inside the molten pool are calculated by solving the following momentum conservation equation.

$$\rho \frac{\partial u_j}{\partial t} + \rho \frac{\partial(u_i u_j)}{\partial x_i} = \frac{\partial}{\partial x_i} \left( \mu \frac{\partial u_j}{\partial x_i} \right) + S_j \quad (3)$$

where  $\rho$  and  $\mu$  are the density and the viscosity of the alloy, respectively,  $u_i$  and  $u_j$  are the velocity components along the  $i$  and  $j$  directions, respectively and  $S_j$  is the source term for  $j$ th momentum conservation equation. Spatial gradient of the pressure field is responsible for the generation of the convective flow of liquid metal inside the molten pool. The following continuity equation is solved in conjunction with the momentum conservation equation to obtain the pressure field.

$$\frac{\partial u_i}{\partial x_i} = 0 \quad (4)$$

The driving forces of the molten metal convection include the surface tension gradient on the top surface of the pool and the buoyancy

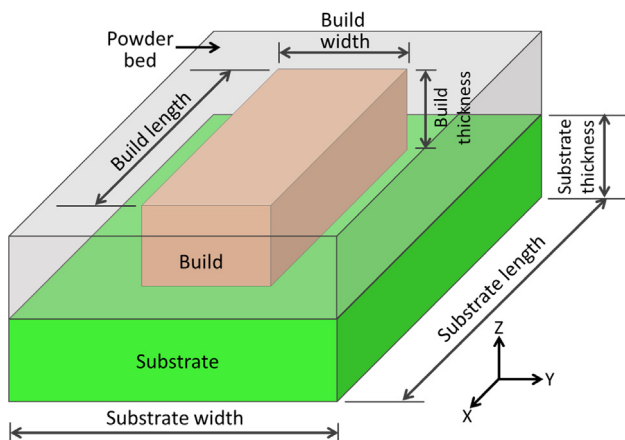


Fig. 1. Schematic of the solution domain consisting of substrate, powder bed and build. X, Y and Z directions represent the scanning, hatching and building directions, respectively.

(gravitational) force [18]. The force due to the surface tension gradient, Marangoni force, is applied as a boundary condition to the momentum conservation equation. The source term in the momentum conservation equation consists of the spatial gradient of pressure field  $\left(\frac{\partial P}{\partial x_j}\right)$  as well as the buoyancy force ( $F_j^b$ ),

$$S_j = -\frac{\partial P}{\partial x_j} + F_j^b \quad (5)$$

Liquid metal flow inside the mushy zone is considered as the flow through a porous medium (according to the Carman-Kozeny equation [19]) where the solids are in the dendritic cell structure. The liquid fraction ( $\phi$ ) in the mushy zone is assumed to vary linearly with temperature between the solidus ( $T_S$ ) and liquidus temperatures ( $T_L$ ) of the alloy [20].

$$\phi = \begin{cases} 1 & T \geq T_L \\ \frac{T-T_S}{T_L-T_S} & T_S < T < T_L \\ 0 & T \leq T_S \end{cases} \quad (6)$$

The pressure gradient responsible for the  $u$  velocity is applied as a source term in the momentum conservation equation and is represented as [21,22]:

$$\frac{\partial P}{\partial x} = -\frac{180 \mu (1-\phi)^2}{\delta^2 \phi^3 + C} u \quad (7)$$

where  $\delta$  is the dendritic cell spacing in microns,  $\mu$  is the viscosity of the liquid metal and  $C$  is a very small computational constant introduced to avoid division by zero. Similar mathematical expressions are also used for  $v$  and  $w$  velocities.

### 2.3. Boundary conditions

At the surfaces of the solution domain, heat exchange takes place between the build and substrate and their surroundings.

$$-k \frac{\partial T}{\partial z} = \sigma \varepsilon (T^4 - T_A^4) + h_c (T - T_A) \quad (8)$$

where  $k$  is the thermal conductivity which is represented by  $k_e$  and  $k_s$  for the solid build and substrate, respectively,  $\sigma$  is the Stefan-Boltzmann constant ( $5.67 \times 10^{-8} \text{ Wm}^{-2} \text{ K}^{-4}$ ),  $\varepsilon$  is the emissivity,  $T_A$  is the ambient temperature and  $h_c$  is the convective heat transfer coefficient.

The convective flow of the molten metal is largely driven by the Marangoni force [17,18] generated due to the surface tension variation on the top surface of the molten pool resulting from the spatial gradient of temperature. On the top surface of the molten pool, the temperature gradient has two components along X and Y directions i.e.  $G_x$  and  $G_y$  respectively. Therefore, the Marangoni shear stresses [18,23,24] along X and Y directions on the top surface of the molten pool can be written as,

$$\tau_x = \mu \frac{du}{dz} = -\frac{d\gamma}{dT} G_x \quad (9)$$

$$\tau_y = \mu \frac{dv}{dz} = -\frac{d\gamma}{dT} G_y \quad (10)$$

where  $\mu$  is the viscosity of the liquid metal. The surface tension of the liquid metal ( $\gamma$ ) depends both on temperature and alloy composition. Most commonly used alloys that do not contain any surface active element have a negative value of  $d\gamma/dT$  [1].

## 3. Numerical solution

### 3.1. Thermo-physical properties

A powder bed consists of both alloy powder particles and the shielding gas within the interparticle space. Therefore, effective

thermo-physical properties of the powder bed depend on both alloy as well as shielding gas properties, size of the powder particles and packing efficiency of the powder bed. The effective density ( $\rho_e$ ) and specific heat ( $C_{p_e}$ ) of the powder bed are written as [25]:

$$\rho_e = \rho_s \eta + \rho_g (1-\eta) \quad (11)$$

$$C_{p_e} = \frac{\rho_s \eta C_{p_s} + \rho_g (1-\eta) C_{p_g}}{\rho_s \eta + \rho_g (1-\eta)} \quad (12)$$

where  $\eta$  is the packing efficiency of the powder bed,  $\rho_s$  and  $\rho_g$  are densities of the solid and gas, respectively and  $C_{p_s}$  and  $C_{p_g}$  are specific heat of the solid and the gas, respectively. The effective thermal conductivity of the powder bed ( $k_e$ ) is calculated following the work by Rombouts et al. [26]:

$$k_e = k_g \frac{\eta N}{2} \left[ 0.5 \ln(1+L) + \ln(1+\sqrt{L}) + \frac{1}{1+\sqrt{L}} - 1 \right] \quad (13)$$

where  $k_g$  is the thermal conductivity of the gas in W/mK,  $N$  is the coordination number and  $L$  is a ratio of a constant and powder particle diameter. The value of the constant depends on the shielding gas type and for Ar its value is  $5.4 \times 10^{-4} \text{ m}^{-1}$ . Temperature dependent thermo-physical properties of the Ar gas [27] and alloy powders [28] are provided in Tables 1 and 2, respectively.

Fig. 2(a) and (b) show the variation of the effective thermal conductivity of the powder bed (stainless steel 316 powder + Ar gas) as a function of temperature for different packing efficiency and powder particle diameter, respectively. Since, thermal conductivities of both the powder particles and Ar gas increase with temperature, the effective thermal conductivity of the powder bed also follows the same trend. For higher packing efficiency, it is easier to transfer heat from one particle to another due to increased area of contact per unit volume. Therefore, effective thermal conductivity increases with packing efficiency as shown in Fig. 2(a). The interparticle space decreases with reduction in particle size. Therefore, the effective thermal conductivity increases with smaller powder particles as shown in Fig. 2(b). At room temperature (300 K), the effective thermal conductivity of the powder bed is around 10 times higher than the thermal conductivity of Ar gas (0.018 W/mK) and 1/100th of the thermal conductivity of stainless steel 316 (16.3 W/mK [28]). Similar values have also been used in the literature [5] to model PBF of stainless steel 316.

Fig. 3(a) and (b) show the variations of temperature, thermal conductivity and specific heat with time for a monitoring location on the top surface of a stainless steel 316 build. The initial temperature at the monitoring location is room temperature (300 K). The thermal conductivity and specific heat at this location are assigned as effective powder bed properties,  $k_e$  and  $C_{p_e}$  respectively. After the laser beam reaches the monitoring location at time  $t_1$ , the temperature at the location exceeds the liquidus temperature of the alloy (1693 K [28]) and the location melts and the thermophysical properties of the liquid are assigned at that location. When the temperature at any location is intermediate between the solidus and liquidus temperature, the thermophysical properties are linearly interpolated between the two temperatures. As the laser beam moves away, the temperature of the location drops to the solidus temperature of the alloy at time  $t_2$  and the location solidifies. Therefore, after time  $t_2$ , thermal conductivity and specific heat at this location are taken as those of the solid alloy. As the location cools both thermal conductivity and specific heat of the location decreases.

**Table 1**  
Thermo-physical properties of Argon gas [27]. Here ‘T’ represents temperature in K.

Properties	Value
Density (kg/m <sup>3</sup> )	0.974
Specific heat (J/kg K)	519.16
Thermal conductivity (W/mK)	$\frac{-0.1125}{\sqrt{T}} + 1.35 \times 10^{-3} \sqrt{T} + 1.453 \times 10^{-7} T^{1.5}$

**Table 2**

Thermo-physical properties of stainless steel 316 and Ti-6Al-4V [28]. Here ‘T’ represents temperature in K ranging from ambient to the solidus temperature.

Properties	Stainless steel 316	Ti-6Al-4V
Liquidus temperature (K)	1733	1928
Solidus temperature (K)	1693	1878
Thermal conductivity (W/m K)	$11.82 + 1.06 \times 10^{-2}T$	$1.57 + 1.6 \times 10^{-2}T - 1 \times 10^{-6}T^2$
Specific heat (J/kg K)	$330.9 + 0.563T - 4.015 \times 10^{-4}T^2 + 9.465 \times 10^{-8}T^3$	$492.4 + 0.025T - 4.18 \times 10^{-6}T^2$
Density (kg/m <sup>3</sup> )	7800	4000
Latent heat of fusion (J/kg)	$272 \times 10^3$	$284 \times 10^3$
Viscosity (kg/m s)	$7 \times 10^{-3}$	$4 \times 10^{-3}$
d $\gamma$ /dT (N/m K)	$-0.40 \times 10^{-3}$	$-0.26 \times 10^{-3}$
Absorption coefficient in liquid ( $\eta_l$ )	0.3	0.3
Absorption coefficient in powder ( $\eta_p$ )	0.7	0.7
Volumetric expansion co-efficient (/K)	$5.85 \times 10^{-5}$	$2.5 \times 10^{-5}$
Young's modulus (GPa)	206	110

Using this method, temperature dependent thermo-physical properties are assigned to all grid points in the solution domain.

### 3.2. Grid system and discretization of the governing equations

The governing equations are discretized in the 3D Cartesian coordinate using the control volume method, where the solution domain is divided into small rectangular control volumes, as shown in Fig. 4. The three components of velocity along X, Y and Z directions are represented as u, v and w, respectively. Dashed lines represent control volume's interfaces and solid dots indicate scalar grid points. A scalar grid point is located at the center of each control volume, storing the values of scalar quantities such as pressure and enthalpy. Grid points w, e, s, n, b, t are of east, west, south, north, bottom, and top neighbors of the grid point P, respectively. The positions of the velocity components are at the control volume faces, staggered with respect to the scalar locations. For example, velocities  $v_s$  and  $v_n$  are placed at the south and north faces of the scalar control volume of the grid point P. Therefore, the discretized governing equation of a variable,  $\Phi$  (enthalpy, velocity or pressure) for a control volume with grid point P is formulated by integrating the equation as [29],

$$a_p \Phi_p = a_n \Phi_n + a_s \Phi_s + a_e \Phi_e + a_w \Phi_w + a_t \Phi_t + a_b \Phi_b + f \quad (14)$$

where ‘a’ denotes the convection-diffusion co-efficients and ‘f’ includes the source terms.

### 3.3. Traveling grid system

Simulation of large components with long tracks, multiple hatches and layers requires a large number of grid points and long computation

time. A conventional fixed grid system where control volumes are specified at the beginning of the calculations and remain fixed throughout the entire simulation process is not very efficient because of the need to have large number of fine grids throughout the calculation domain. Here an adaptive traveling grid system where a fine grid region travels with the moving laser beam is used to simulate large components within a realistic time frame. Fig. 5(a) shows the grid system on the XY plane at the beginning of the building process. The grid is very fine surrounding the laser beam axis so that the entire molten pool is contained inside this fine grid region. Elsewhere, the grids are coarser. The size of the x-grids increase progressively away from the fine grid region. The x-coordinate of a particular x-grid (i) can be written as,

$$x = L_t \left( \frac{i}{N_g} \right)^m \quad \text{for } m > 0 \quad (15)$$

$$x = L_t \left[ 1 - \left( 1 - \frac{i}{N_g} \right)^{-m} \right] \quad \text{for } m < 0 \quad (16)$$

where  $L_t$  and  $N_g$  are the total length of the solution domain and total numbers of grid points, respectively. The grid size varies along the length of the solution domain depending on the value of the constant m. The fine x-grid region travels with the laser beam along the scanning direction (positive x-axis). The number of x-grids ahead and behind the fine grid region are adjusted to keep the total number of x-grids constant. Fig. 5(b) shows the grid system at the end of a particular hatch. For a new hatch, the fine grid region moves back to its initial position (same as Fig. 5(a)). However, when the x-grid shifts for the next step of the laser beam, all calculated variables are to be remapped from the previous grids to the current grids. Fig. 5(c) shows that the grid shifts

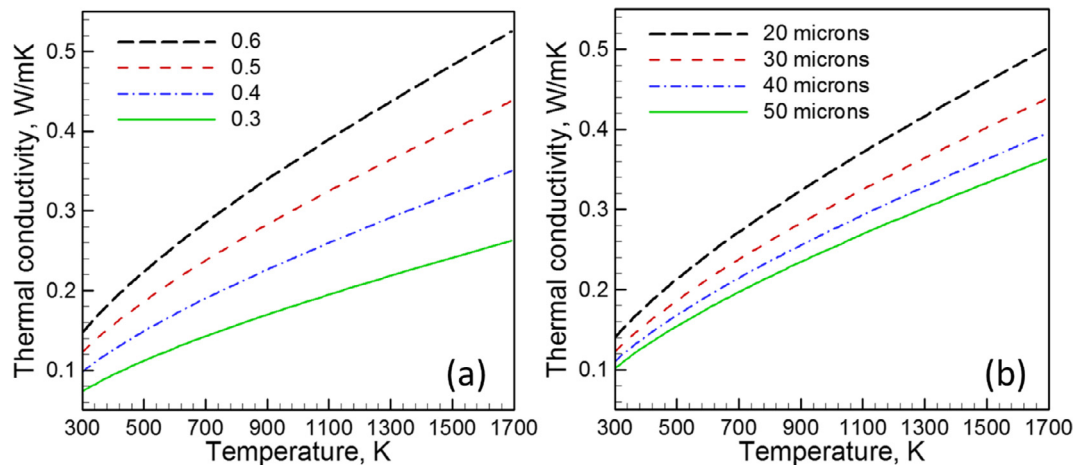


**Fig. 2.** Variation of the effective thermal conductivity of the powder bed (stainless steel 316 powder + Ar gas) with respect to temperature for different (a) packing efficiency of the powder bed and (b) powder particle diameter.

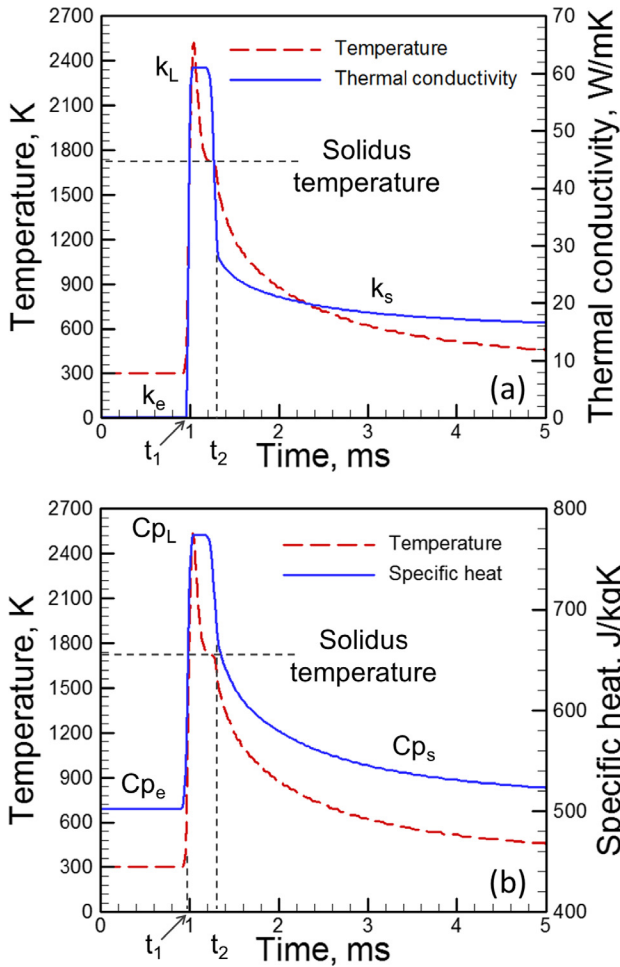


Fig. 3. Variation of temperature and (a) thermal conductivity and (b) specific heat with time for a particular location on the top surface of a stainless steel 316 build using 60 W laser power and 1000 mm/s scanning speed. The suffix ‘e’, ‘L’ and ‘s’ denote the effective properties of powder bed, properties of liquid and powder (or solid), respectively.

from its previous position A'B'C'D' to its current position ABCD. Therefore, a variable,  $\Phi$  for the grid point A,  $\Phi(A)$  can be interpolated from the values at the previous step as,

$$\Phi(A) = \Phi'(A') + \frac{[\Phi'(D') - \Phi'(A')][x(A) - x(A')]}{x(D') - x(A')} \quad (17)$$

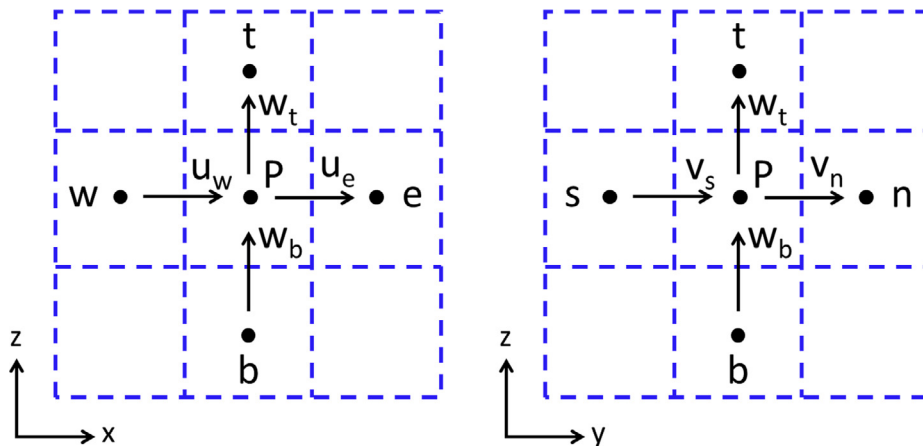


Fig. 4. Grid system using control volume method on (a) XZ and (b) YZ planes of the solution domain. The dashed lines indicate the control volume's interfaces and solid dots represent the scalar grid points. The symbols w, e, s, n, b, t are for east, west, south, north, bottom, and top neighbors of the grid point P, respectively.

where  $x$  denotes the x-coordinate of a particular grid point and the dash in the superscript represents the values of the previous step. Similarly, the values of the variables are calculated for all grid points. Therefore, for a particular grid point ( $i$ ), Eq. (17) can be written as,

$$\Phi(i) = \Phi'(i') + \frac{[\Phi'(i+1)' - \Phi'(i')][x(i) - x(i')]}{x(i+1)' - x(i')} \quad (18)$$

After the variables are interpolated and remapped from the previous to the current grid system, the iterations for the variables are done. The detailed algorithm of grid shift and variable interpolation are given below.

### 3.4. Solution procedure

Fig. 6 is a flow chart showing the computational procedure used. It shows that for a particular layer, the y-location of the laser beam is decided based on the specific hatch and the hatch spacing. The movement of the laser beam is simulated by progressively shifting the beam axis by a very short predetermined distance equal to a small fraction of the laser beam diameter. The time step for the calculation is decided based on that distance and the scanning speed. For a particular step (at a specified x-location) the x-grid is updated and all the variables are interpolated from the grid system of the previous beam location. Based on the updated grids, the governing equations are discretized and the volumetric heat source and boundary conditions are applied. Depending on the temperature field, thermo-physical properties are assigned to all grid points.

All discretized governing equations are simultaneously solved to obtain enthalpy, velocity and pressure fields using a Gaussian elimination technique known as the tri-diagonal matrix algorithm (TDMA) [29]. The temperature field is obtained from the enthalpy field by using temperature dependent specific heat of the alloy. The iterative calculations for enthalpy, velocity and pressure continue until they converge. The calculation continues until all the hatches and layers are completed. These calculations are performed using an in-house Fortran code compiled using an Intel Fortran compiler.

For a 20 mm long, 5 layers, 5 hatches build, the size of the solution domain is 22 mm  $\times$  5 mm  $\times$  3.5 mm (length  $\times$  width  $\times$  height). This domain is divided into 385,000 grid points, where, the number of grids along X, Y and Z directions are 110, 50 and 70, respectively. Among these 110 X-grids, 50 grids are fine traveling grids that cover a region of 0.5 mm and move with the laser beam. The remaining 60 grids are distributed in the coarse X-grid region. Five main variables, temperature, pressure and three velocity components are calculated at each grid points. The continuous scanning of the laser beam for the 20 mm long build is simulated through 2000 small time steps. At each step, about 30

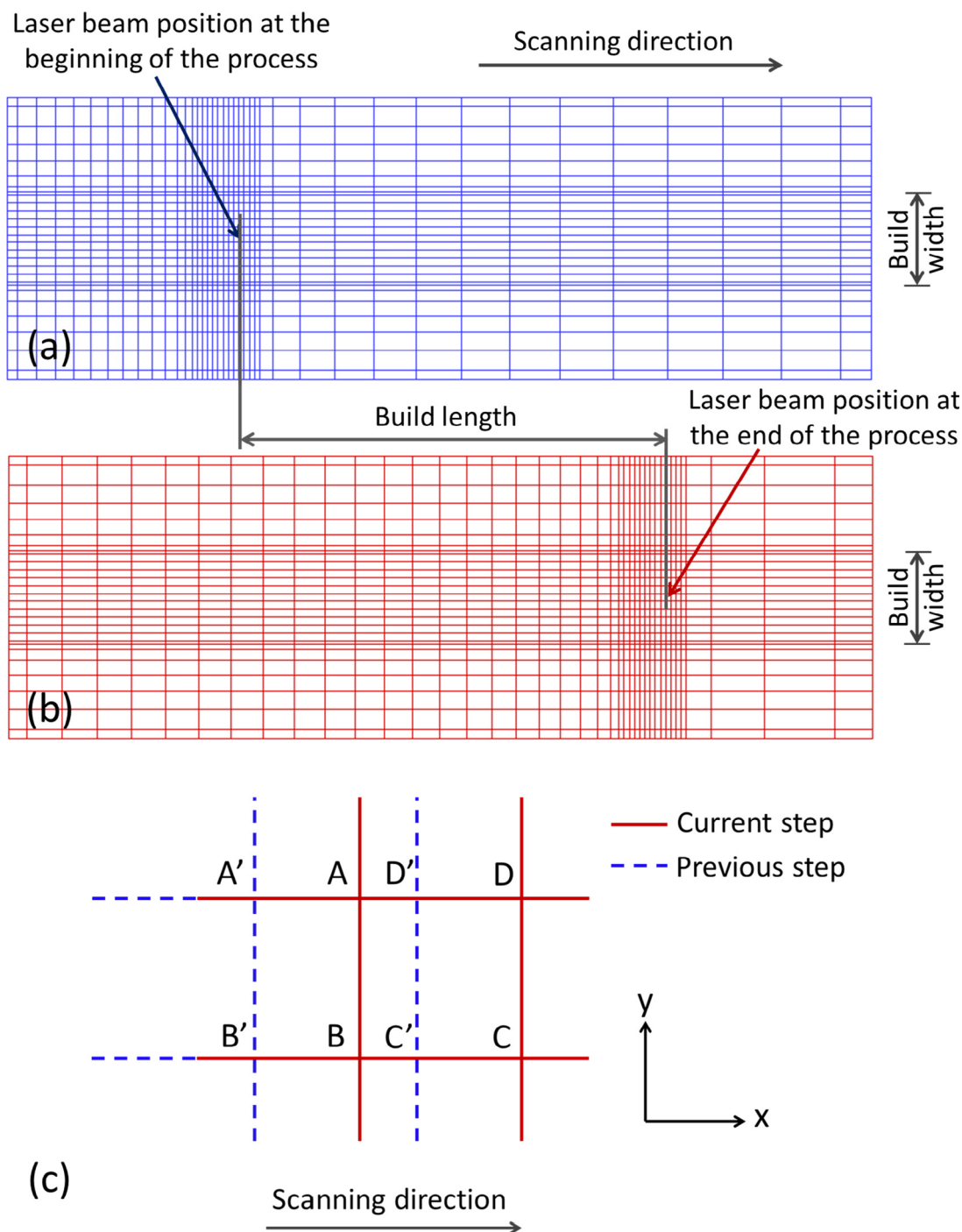


Fig. 5. Schematic representation of the grid system on the top surface of the solution domain at the (a) beginning and (b) end of the process. (c) Schematic representation of the traveling grid where the grid shifts from its previous position A'B'C'D' to its current position ABCD.

iterations are found to be sufficient to achieve fairly good convergence. Therefore, the total number of linear equations being solved for the 20 mm long build with 5 hatches and 5 layers is around  $385,000 \times 5 \times 2000 \times 30 \times 5 \times 5$  (number of grids  $\times$  variables  $\times$  time steps  $\times$  iterations per step  $\times$  layers  $\times$  hatches) =  $3 \times 10^{12}$ . The calculation time is approximately 5 hours for a 5 layers, 5 hatches build in a personal computer with a 3.40 GHz i7 processor and 8 GB RAM.

Fig. 7 shows the simulation time required for different layers in a 20 mm long 5 layers, 5 hatches build. Total number of grid points increases with number of layers. Therefore, the simulation time is higher for the upper layers as shown in Fig. 7. Higher laser power results in larger

molten pool [30] that increases the size of the solution domain for the velocity and pressure calculations. Therefore, the simulation time for processing with a 90 W laser is higher than that that required for a 60 W power. In conventional fixed grid system, fine grids are required for the entire length of the build. As a result, the total number of grid points for the conventional fixed grid system is much more than that required for the traveling grid system. Therefore, the simulation time can be reduced significantly by implementing the traveling grid system.

### 3.5. Stability, convergence and accuracy of solution

The stability of the numerical method described here can be

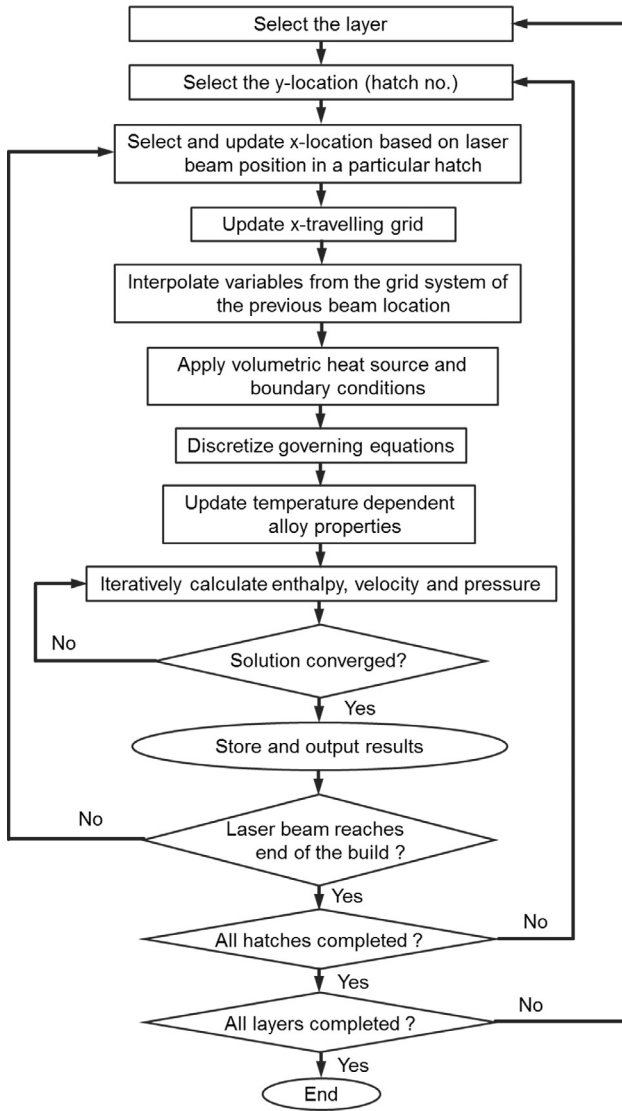


Fig. 6. Schematic diagram showing the overall algorithm of the heat transfer and fluid flow model.

evaluated based on the fluctuation of the output variables such as temperature and velocity with processing time. Fig. 8(a) shows the variation of the pool volume with time for two linear heat inputs (laser power/scanning speed). Higher heat input can melt more materials and form bigger molten pool [30]. With the progress of the process, the molten pool becomes bigger and after a certain time it reaches steady state. After that, the pool volume does not fluctuate with time; therefore, it is a stable solution.

The convergence of the numerical solution is defined based on whether the error (or residue) in the solution is smaller than a specified value. In this numerical method described here, residue for enthalpy ( $R_h$ ) is defined as:

$$R_h = \frac{\sum \left[ \frac{1}{\rho_p} (a_n h_n + a_s h_s + a_e h_e + a_w h_w + a_t h_t + a_b h_b + f) - h_p \right]}{\sum h_p} \quad (19)$$

where the coefficients  $a$  and  $f$  are defined in Section 3.2,  $h$  is the corresponding enthalpy and  $\Sigma$  denotes the summation over all grid points of the solution domain. The residue for u-velocity ( $R_u$ ) is defined as:

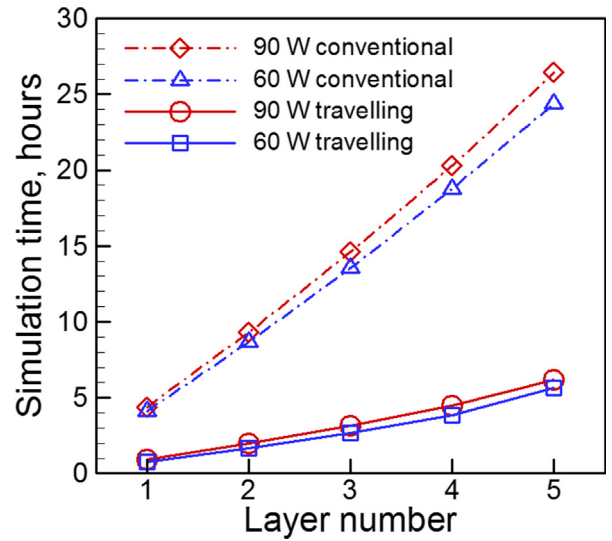


Fig. 7. Simulation time for different layers for a 5 layers 5 hatches stainless steel 316 build with 1000 mm/s scanning speed and 60 W and 90 W laser powers using traveling and conventional fixed grid systems.

$$R_u = \frac{[\sum (a_n u_n + a_s u_s + a_e u_e + a_w u_w + a_t u_t + a_b u_b + f - a_p u_p)] / \xi}{M_{ref}} \quad (20)$$

where the coefficients  $a$  and  $f$  are defined in Section 3.2,  $u$  is the corresponding u-velocity and  $\Sigma$  denotes the summation over all grid points ( $\xi$ ) inside the molten pool. Since, velocities are calculated by solving the momentum conservation equation, a reference momentum,  $M_{ref}$  is used to calculate the velocity residue:

$$M_{ref} = -\frac{d\gamma}{dT} \frac{\rho_L}{\mu} (T_p - T_s) (\lambda r_b) \quad (21)$$

where  $d\gamma/dT$ ,  $\rho_L$  and  $\mu$  are the surface tension gradient, density and viscosity of the liquid alloy, respectively,  $T_p$  and  $T_s$  are the peak temperature and the solidus temperature of the alloy, respectively and  $\lambda$  and  $r_b$  are the layer thickness and laser beam radius, respectively. Similarly, the residues for  $v$  and  $w$  velocities are calculated. When these calculated residues are below a specified value (typically  $\pm 0.1\%$ ), the solution is considered as converged. The calculations are iterated to obtain lower residues and good convergence as shown in Fig. 8(b).

Variations of calculated peak temperature and pool volume with building time are shown in Fig. 9(a) and (b) respectively. Both peak temperature and the solidus temperature increase with building time for a particular hatch and reach steady state after a certain time. The calculated results using the traveling grids match exactly with the results obtained using the conventional fixed grid system for same processing conditions. The agreement provide confidence of using the traveling grid system to achieve better computational efficiency without sacrificing any accuracy. Fig. 9(c) shows the temperature variation with y-distance below the laser beam axis on the top surface of the build. The peak temperature is observed directly below the laser beam axis. The convective flow of liquid metal inside the molten pool mixes hot and cold liquids and reduces the peak temperature from the values obtained from heat conduction calculations where the mixing is not considered [18]. Therefore, the heat conduction calculations result in an unrealistically high peak temperature as shown in Fig. 9(c). Radially outward velocity of the liquid metal increases the molten pool width. Computed temperature fields and molten pool dimensions by considering convective transport of heat provide reliable values of important metallurgical variables such as peak temperature, thermal cycles, cooling rates and solidification parameters [6,17].

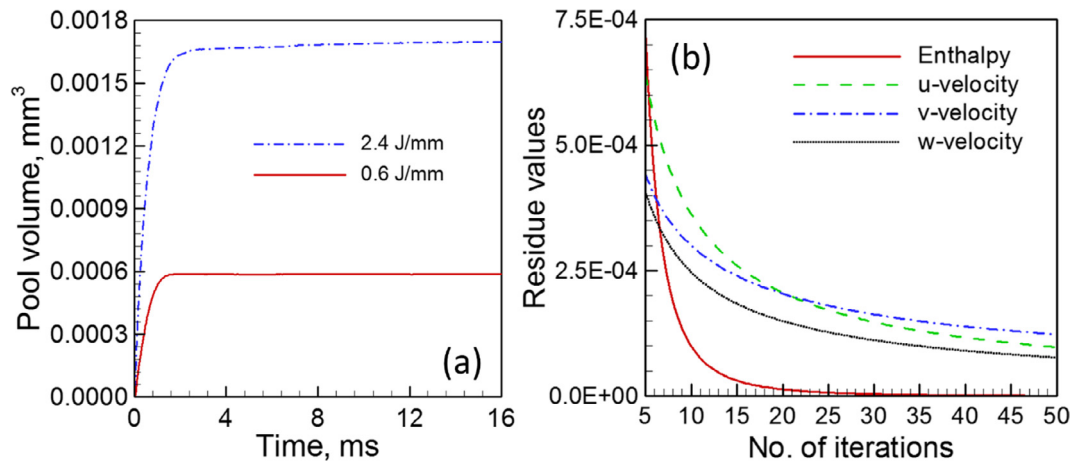


Fig. 8. (a) Variation of pool volume with time for a single layer single hatch stainless steel build using two different heat inputs. (b) Variations of calculated residues or error values with iterations for enthalpy and three components of velocity.

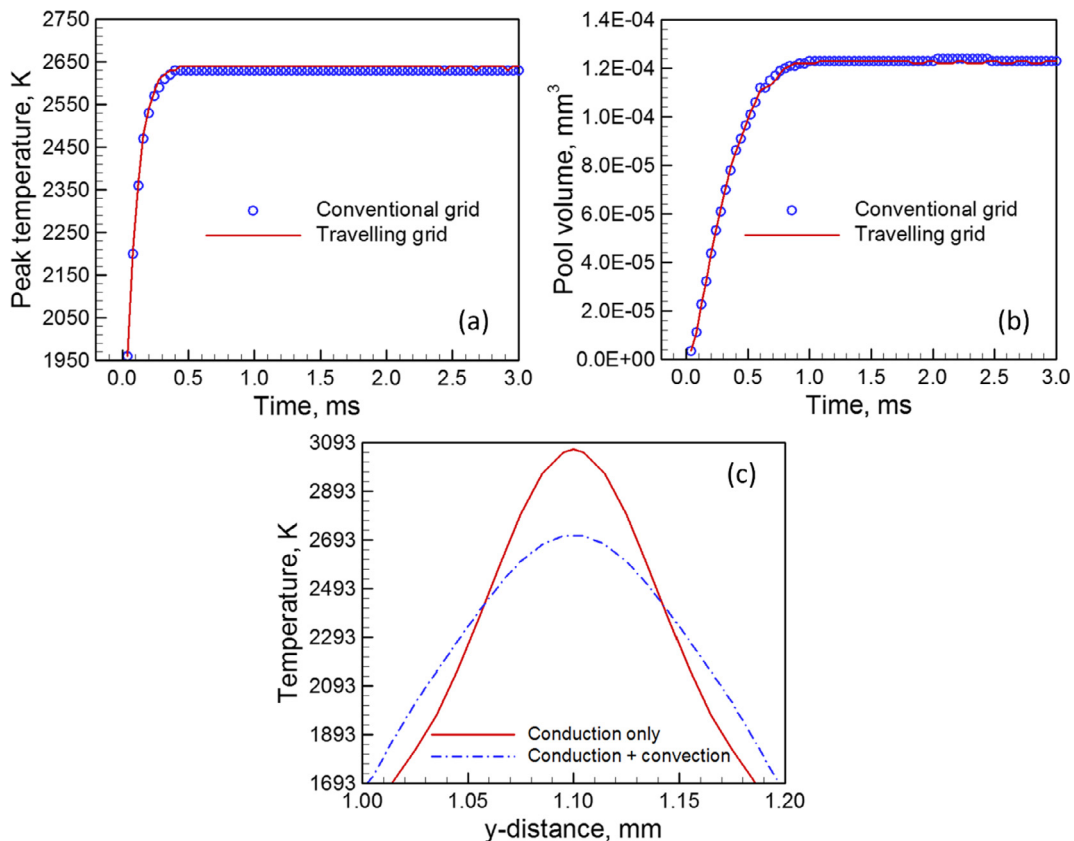


Fig. 9. Comparison of the calculated (a) peak temperature and (b) pool volume with the progress of the building process using traveling grid and conventional fixed grid. (c) Comparison between the temperature variations with y-distance inside the molten pool near laser beam axis ( $y = 1.10$  mm) considering and neglecting convective flow of liquid metal. All plots are for a stainless steel 316 build using 60 W laser power and 250 mm/s scanning speed.

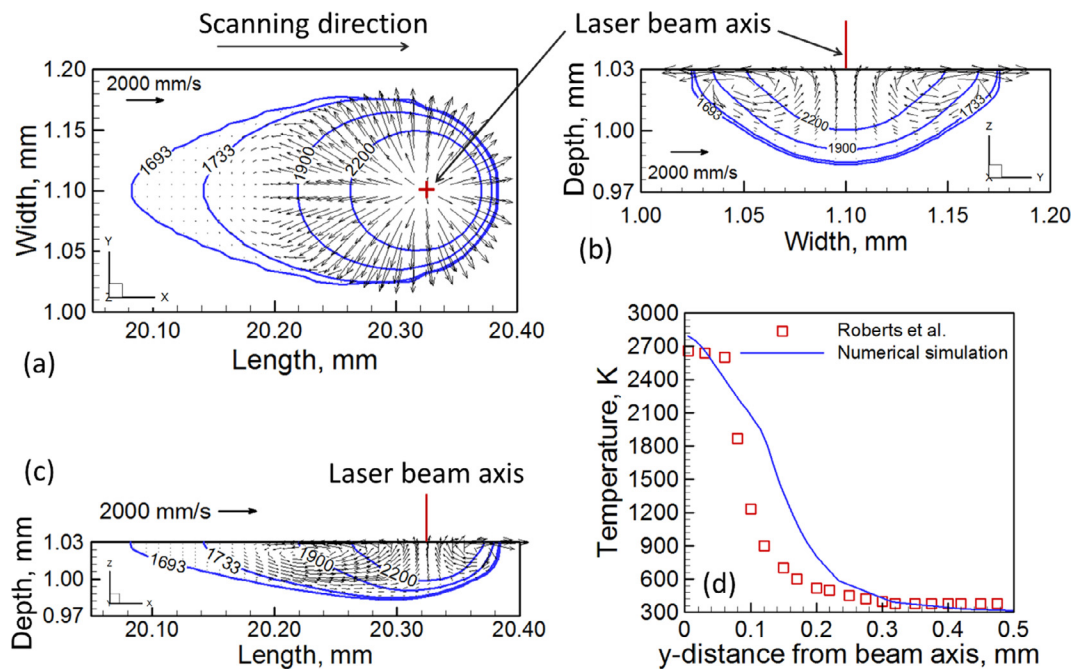
#### 4. Model testing and validation

Fig. 10(a–c) shows the calculated temperature and velocity fields at the 1st layer and 1st hatch of a 20 mm long stainless steel 316 build. The temperature and velocity fields on top (XY), transverse (YZ) and longitudinal (XZ) planes are shown in Fig. 10(a), (b) and (c) respectively. The blue<sup>1</sup> curves represent the isotherms where corresponding temperature values in K are written on them. The liquidus and solidus

temperatures of stainless steel 316 are 1733 K and 1693 K respectively [28]. Therefore, the 1693 K isotherm represents the molten pool boundary. The region between the 1693 K and 1733 K isotherms is the mushy zone. Because of the high scanning speed, the molten pool elongates in the opposite direction of the scanning. The velocity vectors are represented by the black arrows whose magnitude can be found by comparing their length with the reference vector provided. The highest temperature in the molten pool is observed near the laser beam axis. Since, molten metal flows from the high temperature to the low temperature, the velocity vectors are radially outwards.

Fig. 10(b) shows that the temperature decreases with y-distance

<sup>1</sup> For interpretation of color in Fig. 10, the reader is referred to the web version of this article.



**Fig. 10.** Temperature and velocity distributions for the 1st hatch and 1st layer of a 20 mm long stainless steel 316 build on a 24 mm long stainless steel 316 substrate using 60 W laser power and 500 mm/s scanning speed on (a) top (b) transverse and (c) longitudinal planes. The length of the build is from  $x = 2.0$  mm to 22.0 mm. (d) Comparison between numerically calculated and experimentally measured [31] temperature variation with  $y$ -distance from the beam axis for a Ti-6Al-4V build using 120 W laser power and 220 mm/s scanning speed.

from the laser beam axis. Fig. 10(d) shows the variation of temperature with the  $y$ -distance from the laser beam axis for a Ti-6Al-4V build. The calculated results agree fairly well with the independent experimental result by Roberts et al. [31]. The temperature distribution is measured using an infrared camera [31]. Slight mismatch between the experimental and the computed results can be attributed to the complexity of the temperature measurement for a rapidly moving laser beam as well as several simplified assumptions of the model.

## 5. Summary and conclusions

A 3D transient heat transfer and fluid flow model is developed to calculate the temperature and velocity fields, build shape and size and solidification parameters. The main findings from the model development and testing are as follows:

- (1) The thermal conductivity of the powder bed depends on the chemical composition and size of the powder, the powder packing efficiency, the nature of the shielding gas and temperature. The type of shielding gas plays a more important role than the type of metal powder in determining its thermal conductivity. Because of the high temperature sensitivity of the thermo-physical properties, temperature dependent properties are critical for effective simulation of heat transfer and fluid flow in PBF.
- (2) The solution of the equations of conservation of mass, momentum and energy in a domain containing of the substrate, powder bed and solidified build was able to predict the independently measured spatial variation temperature within the Ti-6Al-4V build accurately.
- (3) Convective heat transfer is the main mechanism of heat transfer within the liquid metal pool in the PBF-AM process. Simplified heat conduction calculations ignoring the mixing of the relatively hot and cold liquids significantly over predicts the peak temperature and the temperature gradient in the liquid pool.
- (4) A traveling fine grid-system is capable of providing good convergence, stability and accuracy of the computed transient three-dimensional temperature and velocity fields for large problems with

high computational efficiency and limited memory requirement. For example, a 20 mm long stainless steel 316 component fabricated with 5 layers and 5 hatches is simulated within about 5 hours where the conventional fixed grid model takes around 25 hours to simulate component of similar dimensions in an i7 PC with 8 GB RAM.

An application of the model for investigating laser powder bed AM of four commonly used alloys, stainless steel 316, Ti-6Al-4V, Inconel 718 and AlSi10Mg is discussed in details in part II of this paper.

## Acknowledgements

We acknowledge the support from the US Department of Energy Nuclear Energy University Program grant number DE-NE0008280. One of the authors (T.M.) acknowledges support of an American Welding Society research fellowship, grant number 179466. We also acknowledge helpful discussions with J.S. Zuback and G.L. Knapp of Penn State University.

## Data availability

The raw/processed data required to reproduce these findings cannot be shared at this time due to technical or time limitations.

## References

- [1] T. DebRoy, H.L. Wei, J.S. Zuback, T. Mukherjee, J.W. Elmer, J.O. Milewski, A.M. Beese, A. Wilson-Heid, A. De, W. Zhang, Additive manufacturing of metallic components – process, structure and properties, *Prog. Mater. Sci.* 92 (2018) 112–224.
- [2] G.L. Knapp, T. Mukherjee, J.S. Zuback, H.L. Wei, T.A. Palmer, A. De, T. DebRoy, Building blocks for a digital twin of additive manufacturing, *Acta Mater.* 135 (2017) 390–399.
- [3] T. DebRoy, W. Zhang, J. Turner, S.S. Babu, Building digital twins of 3D printing machines, *Scr. Mater.* 134 (2017) 61–65.
- [4] Y. Li, D. Gu, Parametric analysis of thermal behavior during selective laser melting additive manufacturing of aluminum alloy powder, *Mater. Des.* 63 (2014) 856–867.
- [5] A. Foroozmehr, M. Badrossamay, E. Foroozmehr, S. Golabi, Finite element

- simulation of selective laser melting process considering optical penetration depth of laser in powder bed, *Mater. Des.* 89 (2016) 255–263.
- [6] V. Manvatkar, A. De, T. DebRoy, Heat transfer and material flow during laser assisted multi-layer additive manufacturing, *J. Appl. Phys.* 116 (12) (2014) 124905.
- [7] M. Jamshidinia, F. Kong, R. Kovacevic, Numerical modeling of heat distribution in the electron beam melting<sup>®</sup> of Ti-6Al-4V, *J. Manufact. Sci. Eng.* 135 (6) (2013) 061010.
- [8] P. Yuan, D. Gu, Molten pool behaviour and its physical mechanism during selective laser melting of TiC/AlSi10Mg nanocomposites: simulation and experiments, *J. Phys. D: Appl. Phys.* 48 (3) (2015) 035303.
- [9] C. Korner, A. Bauereiss, E. Attar, Fundamental consolidation mechanisms during selective beam melting of powders, *Model. Simul. Mater. Sci.* 21 (8) (2013) 085011.
- [10] S.A. Khairallah, A. Anderson, Mesoscopic simulation model of selective laser melting of stainless steel powder, *J. Mater. Process. Technol.* 214 (11) (2014) 2627–2636.
- [11] C. Korner, E. Attar, P. Heintl, Mesoscopic simulation of selective beam melting processes, *J. Mater. Process. Technol.* 211 (6) (2011) 978–987.
- [12] Y.S. Lee, W. Zhang, Modeling of heat transfer, fluid flow and solidification micro-structure of nickel-base superalloy fabricated by laser powder bed fusion, *Addit. Manufact.* 12 (2016) 178–188.
- [13] J.S. Turner, *Buoyancy Effects in Fluids*, Cambridge University Press, 1979.
- [14] A. De, T. DebRoy, A smart model to estimate effective thermal conductivity and viscosity in the weld pool, *J. Appl. Phys.* 95 (9) (2004) 5230–5240.
- [15] T. Mukherjee, J.S. Zuback, A. De, T. DebRoy, Printability of alloys for additive manufacturing, *Sci. Rep.* 6 (2016).
- [16] T. Mukherjee, W. Zhang, T. DebRoy, An improved prediction of residual stresses and distortion in additive manufacturing, *Comput. Mater. Sci.* 126 (2017) 360–372.
- [17] V. Manvatkar, A. De, T. DebRoy, Spatial variation of melt pool geometry, peak temperature and solidification parameters during laser assisted additive manufacturing process, *Mater. Sci. Technol.* 31 (8) (2015) 924–930.
- [18] T. DebRoy, S.A. David, Physical processes in fusion welding, *Rev. Mod. Phys.* 67 (1) (1995) 85.
- [19] P.C. Carman, Some physical aspects of water flow in porous media, *Disc. Faraday Soc.* 3 (1948) 72–77.
- [20] S. Kou, *Welding Metallurgy*, second ed., Wiley, Hoboken, New Jersey, 2003.
- [21] N. Poletz, A. François, K. Hillewaert, Multiphysics welding simulation model, *Int. J. Mater. Form.* 1 (2008) 1047–1050.
- [22] W. Zhang, C.H. Kim, T. DebRoy, Heat and fluid flow in complex joints during gas metal arc welding—part I: numerical model of fillet welding, *J. Appl. Phys.* 95 (9) (2004) 5210–5219.
- [23] T. Mukherjee, V. Manvatkar, A. De, T. DebRoy, Dimensionless numbers in additive manufacturing, *J. Appl. Phys.* 121 (6) (2017) 064904.
- [24] T. Mukherjee, J.S. Zuback, W. Zhang, T. DebRoy, Residual stresses and distortion in additively manufactured compositionally graded and dissimilar joints, *Comput. Mater. Sci.* 143 (2018) 325–337.
- [25] Y. Zhang, A. Faghri, Melting and resolidification of a subcooled mixed powder bed with moving Gaussian heat source, *J. Heat Trans.* 120 (4) (1998) 883–891.
- [26] M. Rombouts, L. Froyen, A.V. Gusarov, E.H. Bentefour, C. Glorieux, Photopyroelectric measurement of thermal conductivity of metallic powders, *J. Appl. Phys.* 97 (2) (2005) 024905.
- [27] T. Hoshino, K. Mito, A. Nagashima, M. Miyata, Determination of the thermal conductivity of argon and nitrogen over a wide temperature range through data evaluation and shock-tube experiments, *Int. J. Thermophys.* 7 (3) (1986) 647–662.
- [28] K.C. Mills, *Recommended Values of Thermo-Physical Properties for Selected Commercial Alloys*, Woodhead Publishing, Cambridge, 2002.
- [29] S.V. Patankar, *Numerical Heat Transfer and Fluid Flow*, McGraw-Hill, New York, 1982.
- [30] T. Mukherjee, V. Manvatkar, A. De, T. DebRoy, Mitigation of thermal distortion during additive manufacturing, *Scripta Mater.* 127 (2017) 79–83.
- [31] I.A. Roberts, C.J. Wang, R. Esterlein, M. Stanford, D.J. Mynors, A three-dimensional finite element analysis of the temperature field during laser melting of metal powders in additive layer manufacturing, *Int. J. Machine Tools Manuf.* 49 (12) (2009) 916–923.